In-situ dynamic WetSEM imaging and electrical impedance measurements on Portland cement during early hydration

In-situ dynamic WetSEM imaging and electrical impedance measurements on Portland cement during early hydration

Benny Suryanto*, James O. Buckman, W. John McCarter, Hussameldin Taha

School of Energy, Geoscience, Infrastructure and Society,

Heriot-Watt University,

Edinburgh, EH14 4AS,

United Kingdom,

* Corresponding Author

E-mail: b.suryanto@hw.ac.uk

Tel: +44 (0)131 451 3817

Fax: +44 (0)131 451 4617

ORCID:

Benny Suryanto: 0000-0002-3979-9994

William J McCarter: 0000-0002-1949-2856

Highlights

- Dual testing methodology for *in-situ* monitoring of early hydration presented
- Automated image collection applied to the WetSEM technology for the first time
- WetSEM images correlate with data from electrical impedance measurements
- Portlandite precipitation alters both conduction and polarization processes
- Double-layer and interfacial processes give rise to the bulk polarization

Abstract

Wet scanning electron microscopy (WetSEM) and electrical impedance measurements have been employed to study the physico-chemical processes during the early hydration of Portland cement. The WetSEM study employed the Quantomix WetSEM capsule, allowing examination of the morphology of hydrating cement directly *in situ* via 36 semi-electron-transparent windows under SEM vacuum conditions over the initial 24-h after gauging whilst maintaining the test sample under atmospheric conditions. This qualitative assessment was used to aid interpretation of the stages of early hydration identified from impedance measurements, which were taken on a replicate specimen over the frequency range 1kHz–1MHz. It is shown that detailed frequency- and time- domain impedance measurements allowed identification of key processes during setting and early hardening which were correlated with data from the WetSEM study. Attention is directed to the sequence of hydration obtained from the two techniques and how they provide both supporting and complementary information.

Keywords: early hydration; electrical properties; cement; WetSEM; electrical impedance.

1. INTRODUCTION

Cement hydration is a dynamic process involving a series of complex and interrelated physico-chemical processes taking place immediately from gauging throughout setting and early hardening. Given that the early hydration of cement is exothermic by nature, these processes have been traditionally studied using isothermal conduction calorimetry and adiabatic temperature rise testing [1-6]. These methods do not, however, provide direct information on microstructural changes which are more relevant to long-term durability and performance of concrete. More advanced techniques have been employed in this respect, including environmental scanning electron microscopy (ESEM), transmission electron microscopy, nuclear magnetic resonance, ultrasonic pulse velocity, X-ray diffraction and X-ray tomography [see, for example, 7-15].

In terms of microstructural changes during early hydration, the present work employs the WetSEM technology [16] whereby a hydrating cement paste is continuously imaged under atmospheric conditions within an *environmental* capsule inside a scanning electron microscope (SEM) over a 24-h period after gauging. In traditional SEM operation, examination of cement hydration is generally made by stopping the hydration process at various stages, typically by plunging in liquid nitrogen or by high-pressure freezing before examination by cryo-SEM [17, 18]. Such studies are important as they address information on the physical changes of cement hydration over time. However, the action of freezing the hydration process, particularly plunge freezing, may introduce artefacts and not provide a true reflection of hydration processes in its natural state. To address this issue, the environmental SEM (ESEM) was developed to provide a high-resolution method of studying cement in its wet state [19-21]. However, artefacts can still be introduced during chamber pump-down and maintaining samples hydrated during hydration and curing, with associated exothermic reactions, has been proven to be difficult. This has led to the development of the WetSEM technology through the use of a WetSEM capsule (viz, the Quantomix [16, 22]). In essence, a WetSEM capsule offers a sealed micro-environment, impervious to vacuum, with access to the hydrating test sample through a series of semi-electron-transparent windows. As such, it is possible to minimize artefacts introduced

as a consequence of vacuum as in normal SEM operation. Such capsules are particularly useful for a range of materials, including biological specimens, pharmaceutical and hydraulic materials [16, 23-24].

In-situ dynamic imaging of cement hydration using WetSEM technology has now been demonstrated by several researchers. Katz et al. [16] was the first to employ this technology to follow the dynamic nature of the hydration process of gypsum and cement paste at varying water-to-binder ratios, with observations undertaken at magnifications up to 20k×. Whilst the study was carried out over a 24-h period, only interpretations at 6-h and 24-h of hydration were presented, with a highlight being made on the presence of Portlandite at 6-h and the development of calcium-silicate-hydrate (C-S-H) around cement grains, when observed at the end of the test period (24-h after gauging). The use of WetSEM at a prolonged exposure and higher magnifications than 10k× was not recommended as it can generate extra heat which may accelerate the hydration process. Gallucci and Scrivener [25] further discussed the strengths and limitations of the technology and highlighted the importance of sample preparation for successful imaging. In their study, repeated low-magnification observations were made to highlight the sequence of hydration during the early age and the precipitation of C-S-H was found not only around cement grains but also in the pore space between the grains. Hexagonal Portlandite was found to precipitate at less than 3 hours, which then eventually blocked the observation window at ~13-h, possibly due to prolonged beam heating. To minimize extra heat from the electron beam, Venkiteela and Sun [26] employed the blank beam function in a SEM to facilitate repeated observations on a 15-min cycle during the initial eight hours after gauging. In their study, cement pastes with varying water-to-cement ratios were contained within WetSEM capsules and the images obtained from the repeated observations were then processed using image analysis. It was found that the water volume decreases with increasing hydration time while the total solid volume shows an opposite trend, which was interpreted as particle growth.

The primary aim of the present work is to employ two different, yet complimentary, experimental techniques:

(i) WetSEM, with the aim of providing qualitative information on the morphology of the hydration products during the initial stages of hydration; and,

(ii) Electrical property and internal temperature measurements [27], with the aim of providing quantitative information on the physico-chemical processes occurring during early hydration.

Regarding (i), an automated technique employing the WetSEM capsule is introduced for the first time to obtain time-lapse images of the physical and morphological changes within the paste throughout setting and early hardening. Regarding (ii), monitoring the electrical properties of cementitious systems represents a relatively simple testing technology to study setting and hardening under non iso-thermal conditions; samples are not necessarily restricted to cement pastes and mortars, concretes can also be studied [27, 28], thereby offering the potential for deployment in real-world concreting operations [29]. These two techniques differ in the information they provide and this paper attempts, for the first time, to correlate measurements obtained from WetSEM imaging with electrical impedance measurements.

2. EXPERIMENTAL PROGRAMME

2.1 Materials and sample preparation

The cement paste was prepared using CEM I 52.5N to EN197-1 [30] (see the typical oxide composition in Table 1) and mains tap-water with a resistivity of ~160 Ωm. These two materials were mixed at a relatively high water-to-cement ratio (w/c=0.55) to ensure sufficient consistency for the WetSEM study, detailed below. All test samples were produced from the same bag of cement to minimize the influence of variability of materials on test results. The cement bag and the mixing water were pre-conditioned in a temperature controlled laboratory (22±1^{o}C) for more than 24-h prior to the start of testing.

During the production of the sample for the WetSEM study detailed below, 0.5-litres of cement paste was hand mixed for 2-min and an aliquot was then pipetted into a Quantomix QX-102 capsule (see Fig. 1(a)). The capsule comprised two main parts: an upper cell into which the paste was injected and

a sealing stub which formed the base of the capsule. These two parts were connected by a flexible rubber packing to ensure air and water tightness, as well as relieving excessive pressure during cell closure. The upper cell had a semi-electron-transparent thin membrane, reinforced with metal grid to provide the required strength to withstand the pressure difference while under vacuum in the SEM. The metal grid divided the top membrane into 36 equally-sized semi-electron-transparent windows, resulting into an arrangement displayed in Fig. 1(b). In this figure, the white grid corresponds to the metal supporting frame whereas the black rounded squares represent the observation windows. It is through these windows that continuous imaging of the physical changes in the paste, which was in contact with, or in close proximity to, the inner surface of the membrane was possible, as it hydrated under atmospheric conditions.

Together with the sample for the WetSEM study, a paste specimen with the same w/c ratio was prepared for electrical measurements using a 2-litre Hobart planetary motion rotary mixer. The paste was mixed for 2-min before being compacted into a Plexiglas cuboidal cell with internal dimensions $50\times50\times50$ mm^3 (see Figure 1(c)). Following a previous study [27], a pair of stainless steel pins (grade 316L), each 2.4 mm in diameter, were embedded centrally inside the cell to a depth of 25 mm with a centre-to-centre spacing of 25 mm. Immediately after compaction, the top surface of the cell was covered with a plastic film to minimize evaporation and the cell was then contained within a benchtop climatic chamber at a temperature of 22°C and relative humidity of 95%.

2.2 Measurements and data processing

Scanning electron microscope. A Quanta 650 field-emission gun scanning electron microscope (FEI, Hillsboro, US) fitted with an Oxford Instruments X-max^N 150 mm Energy Dispersive X-ray (EDX) detector was used for the study. Before starting the imaging sequence, one WetSEM capsule containing a freshly prepared paste was positioned onto the stage of the SEM, with the cell membrane facing the electron beam. Imaging was then taken using a backscattered electron (BSE) detector in high vacuum mode, with the SEM operating at 20 kV using a spot size of 5.2 and a working distance of 10mm [31].

Automated image acquisition was performed 10 minutes after gauging, using the FEI MAPS software (Version 2.1, 64-bit, FEI). The mapping process involved the acquisition of a series of BSE images across a regular tile pattern, following the sequence described in the schematic shown in Figure 1(d). From each individual tile, high resolution 4096×4096 (16M) pixels low magnification (600×) BSE image was acquired, starting from Tile 1 (top left) and then moving systematically from left-to-right and top-to-bottom toward Tile 36 (bottom right). At this resolution, it took approximately 35-min to obtain the image of the entire area (36 tiles). The same mapping process was then repeated until 24-h after gauging (or 42 times), producing a total of 1,512 images. The advantages of acquiring images in this manner are threefold:

(i) a reduction in the electron beam exposure which minimizes local heating and hence the risk of membrane failure due to electron beam heating;

(ii) minimize the additional heat generated by the electron beam thereby reducing its influence on the physico-chemical processes during the early hydration; and

(iii) generate 36 notionally identical samples from a single experiment run, allowing the evaluation of the inherent variability among the samples whilst maintaining the quality of individual images.

On completion of experiment, the individually acquired images were manually aligned using the GIMP software (Version 2.8.10) to form a time-lapse complete montage of the paste (see, for example, Fig. 2). The images were further processed to create GIF animations which are provided as a video component to the electronic version of this article.

Electrical measurements. An E4980AL high-precision LCR meter (Keysight, Santa Rosa, US) was used to perform a logarithmic impedance sweep at 61 spot frequencies within the range 1kHz-1MHz, under a signal amplitude of 350 mV. The LCR meter was controlled by a desktop PC using a custom-designed virtual instrument in LabVIEW (Version 2015, National Instruments, Austin, US). Communication with the LCR meter was established across a USB interface using Keysight IO Library Suite software (Version 2017.1). Electrical measurements were undertaken by connecting the electrodes to the voltage high/low and current output/input terminals in the LCR meter via

individually screened coaxial cables, with connection at the electrodes by means of alligator clips. Measurements were undertaken in voltage-drive mode on a four-minute cycle throughout the initial 24-h after gauging. One measurement cycle over the full frequency range took approximately 15-s. The LCR meter was placed in standby mode between measurement cycles until the next measurement was triggered.

Lead inductive effects were *nulled* from the measured impedance response using a measurement correction protocol implemented in Microsoft Excel; full details of the protocol are provided elsewhere [32]. Two sets of calibration data were acquired prior to the start of experiment, comprising

(i) An open-circuit correction, with sweep measurement taken with the coaxial cables connected to the pin electrodes positioned within an empty cell; and

(ii) A short-circuit correction, with sweep measurement taken on the same setup, but with the electrodes being short-circuited.

In addition to impedance measurements, the internal temperature of the test specimen and the climatic chamber were monitored every 2 minutes using a 5K thermistor via an auto-ranging data logger.

2.3 Preliminaries for electrical measurements

The electrical properties of a porous, saturated cementitious material rely on the ease with which charges can contribute to conduction and polarization processes within the system and depend, primarily, on the frequency of the applied electrical field and the time-variant nature of both the evolving pore structure and pore-fluid chemistry [33, 34]. To provide a detailed insight into chemical reactions, microstructural changes and pore structure development within a cement paste, these measurements are taken over three orders of magnitude of frequency (viz, 1kHz–1MHz).

From an electrical standpoint, the impedance, $Z(\omega)$, of a material at any angular frequency, ω, can be written as,

$$Z(\omega) = Z'(\omega) - iZ''(\omega) \quad (1)$$

where $Z'(\omega)$ is the resistive (real) component (in Ohm), $Z''(\omega)$ is the reactive (imaginary) component (in Ohm), $i = \sqrt{-1}$ and $\omega = 2\pi f$ with f being the frequency of the applied field (Hz). At any frequency, the electrical response of such a system will result from the superposed phenomena of conduction and polarization which can be quantified, respectively, by the bulk conductivity, $\sigma(\omega)$ (S/m), and the relative permittivity, $\varepsilon_r(\omega)$. These parameters can be de-embedded from the resistive and reactive components by [35],

$$\sigma(\omega) = \left(\frac{Z'(\omega)}{Z'(\omega)^2 + Z''(\omega)^2}\right)\frac{L}{A} \quad (2)$$

$$\varepsilon_r(\omega) = \frac{1}{\varepsilon_o \omega}\left(\frac{Z''(\omega)}{Z'(\omega)^2 + Z''(\omega)^2}\right)\frac{L}{A} \quad (3)$$

where ε_o is the permittivity of a vacuum (8.854×10^{-12} Farads/m) and L/A (/m) is a factor which is related to the electrode geometry and sample configuration. As the electrical field between the electrodes is non-uniform, the geometrical constant L/A in above equations cannot be readily calculated. This was thus determined by impedance measurements on a liquid of known conductivity placed within the same test cell. For the electrode arrangements and test cell used in the current work, the geometrical factor L/A was evaluated as 34.92 m^{-1}. Given that the relative permittivity calculated using Eq. 3 can extend over several orders of magnitude, the term normalised permittivity, denoted $\varepsilon_N(\omega)$, is introduced to aid comparative analysis. This is defined as $\varepsilon_{r,t}(\omega)/\varepsilon_{r,o}(\omega)$, with $\varepsilon_{r,o}(\omega)$ representing the measured permittivity at the start of the test and $\varepsilon_{r,t}(\omega)$ representing the corresponding value measured at time, *t*, after the start of the test.

3. TEST RESULTS AND DISCUSSION

3.1 *In-situ* dynamic imaging

To provide a qualitative assessment of early hydration process, Figs. 2(a)–(d) present a complete montage of the 36 individually acquired BSE images at four selected points in time during the 24-h period. In the initial state displayed in Fig. 2(a), the bright dots correspond to the upper part of the cement grains which was in close proximity or in contact with the inner surface of the semi-electron-transparent membrane. The dots are surrounded by darker regions which occupy a larger fraction of

247 the observation windows and represent the interstitial aqueous phase between the cement grains. In
248 some windows, the appearance of one to two large dark regions is evident, corresponding to the
249 presence of occluded micro air voids which have adhered to the inner side of the membrane. Thin
250 horizontal and vertical lines extending across the entire image are evident which indicate the grid/tile
251 boundaries (see the gridlines in Fig. 1(d)). It is apparent from Figs. 2(a)–(d) that the vertical gridlines
252 become progressively displaced to the right due to slight inherent drift in the electron beam. This does
253 not, however, impair the usability of the proposed technique as the individually collected BSE images
254 can be stitched together to construct the montage. Given the large area to scan and the considerable
255 time required to follow the dynamic nature of the hydration process, it is essential to ensure that the
256 electron beam source is stable, with regard to BSE intensity. This is required to remove inadvertent
257 variance in BSE intensity which would render interpretation of the results difficult. The results
258 presented in Figs. 2(a)–(d) reveal that this is not an issue as all windows within each figure display
259 comparable brightness with no notable variations in BSE intensity levels.
260
261 With reference to Figs. 2(a)–(d), it is evident that as hydration reactions progress, the water level
262 within the capsule subsides with time revealing a porous surface comprising partially hydrated cement
263 grains which are bright and pore space which is dark (see Figs. 2(c) and (d)). At the same time, the
264 interstitial pore space is also progressively filled by hydration products although most of this space is
265 covered by water which is not electron transparent and hence most of this infilling process remains
266 undetectable. Another prominent feature from Figs. 2(c) and (d) relates to the presence of large,
267 elongated, bright crystals of Portlandite which are scattered over the top surface of the paste. The
268 amount and geometry of this crystal formation varies from one window to another and would be
269 indicative of inherent variability in the available pore space between the cement grains and in the
270 concentration of Ca^{2+} in the interstitial aqueous phase.
271
272 To provide a better insight into the process of cement hydration, the complete time-lapse BSE images
273 for Window 14 (3-6 in Fig. 1(b)) are displayed in Fig. 3. This is also provided as a video component
274 to the electronic version of this article; to access this video component, simply click on the image

visible below (see Video 1 in the electronic version of this article). As before, the upper part of the cement particles which was in close proximity or in contact with the membrane was observed as bright dots, whereas the liquid covering the remainder of the particles is shown as dark areas. No obvious differences in morphology are evident during the initial state i.e. the first three images, indicating that there have been no significant physical changes to the cement grains when observed at this low magnification. The first prominent feature can be seen from ~1-h 45-min after gauging, or image 4 on Fig. 3 where the precipitation of elongated, calcium-rich crystals (i.e. Portlandite) are evident in the water-filled capillary space between the grains, as indicated by the circle in image 4 (Fig. 3). The nucleation of Portlandite at this early age agrees with the findings of Gallucci and Scrivener [25] although in their study this was observed at a later stage (~3-h after gauging). Marked crystal growth is evident from the successive images displayed in Fig. 3, transforming into a *massive* crystal which is angular in shape with smooth sides and some perforations. To highlight the growth process, enlarged images of the area indicated by the rectangles in images 8, 14, 21 and 32 in Fig. 3 are presented in Figs. 4(a)–(d); for clarity, the lime-lapse images of this crystal growth are also included as Video 2 in the electronic version of this article. The nucleation of similar crystals but varying in size and shape is evident in Fig. 3 throughout the 24-h test period. Apart from Portlandite, the precipitation of much smaller hydration products is also apparent on the grain surface (see, for instance, Fig. 4(d)) and is discussed below. It is also evident from Fig. 3 that the exposed surface of the cement grains (the bright dots) becomes brighter and the free water-content of the paste reduces with time, which is indicative of water consumption resulting from the hydration reactions and could give a false impression of particle growth viz. the gradual decrease in water-level is interpreted exclusively as particle growth.

Another notable feature from Fig. 3 (and Video 1) is related to the increasing rate of reduction in free water-content resulting from the hydration reactions from ~8-h (image 14), thereby exposing the underlying structures comprising partially hydrated cement particles and capillary pores (dark regions). This is highlighted on the image by the two circled areas, with the enlarged version displayed in Figs. 4(e) and (f). As hydration progresses, the free water-content continues to reduce,

most notably from ~10-h after gauging (see image 18 onwards on Fig. 3), signifying a period of chemical activity. The result is a porous surface which has been depleted of water, giving a *coral reef* appearance.

Fig. 5 displays BSE images of Window 2 (1-4 on Fig. 1(b)) at six selected times over the 24-h test period, with four enlarged images at 24-hours presented in Figs. 6(a)–(d) and the corresponding video component included as Video 3 in the electronic version of this article. It is evident from Fig. 5 that the sequence of events is comparable to those presented earlier in Fig. 3, although the time that corresponds to a particular event varies to some extent from one window to another indicating the temporal and spatial variations in hydration response. This includes: (i) the time at which the Portlandite starts to crystalize; and (ii) the time when the interstitial aqueous phase starts decrease. Fig. 8, for clarity, presents the respective times for each window at which Portlandite appears and the decreasing free water-content process starts; the mean values were found to be, respectively, 2-h 15-min with a coefficient of variation (CoV) of 33% and 8-h 25-min with a CoV of 20%.

With reference to the enlarged images taken at 24-h, it is evident from Figs. 6(a)–(d) that the large Portlandite crystals are surrounded by cement grains covered by fibrillar outgrowths comprising C-S-H and some longer, needle-like (ettringite) crystals [15, 17, 21, 36, 37]. To highlight the growth process of these crystals, Figs. 7(a)–(f) present the time-lapse of Fig. 6(d) at 2.5-h, 4-h, 6.5-h, 8-h, 10-h and 12.5-h after gauging, with the complete time-lapse provided as Video 4 in the electronic version of this article. No notable outgrowth from the grain surface are apparent at 2-h (Fig. 7(a)), although local precipitation may have occurred on the grain surface (see, for instance, [17]). However, this remains undetected as it is beyond the resolution of the acquired BSE image. Notable outgrowths are evident from ~4-h after gauging (Fig. 7(b)), with a more rapid outgrowth detected from ~6.5-h after gauging (Fig. 7(c)), which continued over the remainder of the test period (viz, Figs. 6(d) and 7(d)–(f)). To obtain more detailed insights into the hydration processes on the grain surface, further research involving the freezing of cement paste sample at various stages of hydration and further examination by cryo-SEM is required.

Figs. 9(a) and (b) present, respectively, the BSE images and elemental EDX maps of Windows 11, 12, 17, 18, 24 and 25 (see Fig. 1(d)) at 24-h after gauging. Figs. 9(c) and (d) present an enlargement of the selected area shown in Window 18 (on Fig. 9(a)) and the respective elemental EDX map whose spectra are presented in Fig. 9(e). The map indicates that the large bright crystal displayed in the BSE image in Fig. 9(c) is calcium rich which agrees with the strong peak of calcium in Spectrum 1 (Fig. 9(e)), indicating Portlandite. Spectrum 2, representing the darker area in Fig. 9(c), displays strong peaks due to calcium and silicon from calcium-silicate-hydrate (C-S-H) [38] (similar to the precipitates covering the cement grains presented earlier in Figs. 6(c)), and weak peaks due to aluminium and sulphur from monosulphoaluminate (AFm) and ettringite (AFt) [38]. While hydrogen is a key component in C-S-H, it does not appear in the elemental analysis as it has only one electron-shell, and hence is not X-ray reflective. Spectrum 3 displays strong peaks due to silicon from the silicate phase in the cement and other peaks due to calcium, aluminium, potassium and sulphur. Spectra 4, 5 and 6 display strong peaks due to calcium, aluminium and silicon and weak peaks due to magnesium, sulphur, potassium and iron, suggesting the presence of partially hydrated aluminate and ferrite crystals covered by hydrates comprising C-S-H and ettringite (AFt) [38, 39].

3.2 Electrical property measurement

3.2.1 Preliminaries

Immediately on gauging, cement and water takes the form of a heterogeneous colloidal suspension which gradually turns into a solid matrix through a series of complex physico-chemical processes. Under the action of an alternating electrical field, some charges (ions in solution) are free to drift through the continuous aqueous phase and discharge at the electrodes, producing an ionic conduction effect. Other charges, which are electrostatically held onto grain or gel surfaces, oscillate about their zero-field equilibrium position in sympathy with the alternations of the electric field. This can induce large dipole moments which increases the overall polarizability of the system (see Fig. 10(a)). This is a low-frequency polarization mechanism and generally referred to as the double-layer polarization [40, 41]. In addition to this mechanism, albeit operating over an intermediate frequency (high kHz–MHz), is an interfacial polarization process [42] which is schematically shown in Fig. 10(b). As

hydration progresses, free charges in the aqueous phase may accumulate at internal interfaces within the material; whilst such charges do not contribute to the overall ionic conduction process, it increases the polarizability of the paste. The polarizability of the system can be quantified by the relative permittivity (Eq. 3) whereas the conductive effect can be quantified by the bulk conductivity (viz, Eq. 2). Given that both parameters are influenced by free and bound charges, the measurement of both parameters throughout setting and hardening processes could offer detailed insights into the dynamic, time-variant nature of early hydration.

3.2.2 Interpretation of test results

To provide a quantitative assessment of the physical changes and chemical processes during the early hydration process, the electrical response of the cement paste is discussed below. For clarity, only every 10^{th} data marker is highlighted on Figs. 11(a)–(c).

Fig. 11(a) presents the change in the conductivity, $\sigma(\omega)$, over the 24-hour test period together with its derivative, $d\sigma/dt$, with the conductivity presented at a frequency of 100kHz. This frequency was found high enough to ensure that the influence of electrode polarization was negligible (discussed below), thereby allowing accurate evaluation of the bulk response. The change in normalised relative permittivity, $\varepsilon_N(\omega)$, during the same test period is presented in Fig. 11(b). While data were measured at 20 frequencies per decade over the frequency range 1kHz–1MHz, $\varepsilon_N(\omega)$ is only presented at five spot frequencies viz. 1kHz, 100kHz, 250kHz, 500kHz and 1MHz, with $\varepsilon_{r,o}(\omega)$ presented in Table 2. In general terms, the conductivity increases up to ~1-h 40-min and then decreases over the remainder of the test period, with a weakly developed *shoulder* detected between 8-h and 12-h. $\varepsilon_N(\omega)$ measured at 1kHz, 100kHz and 250kHz (Fig. 11(b)) displays a similar trend to the conductivity, with the shoulder becoming more prominent with increasing frequency of applied field. The shoulder is, however, absent at higher frequencies (viz, 500 kHz and 1 MHz) and $\varepsilon_N(\omega)$ displays a monotonic increase from ~8-h.

On closer examination, the conductivity response and its derivative, $d\sigma/dt$, can be further subdivided into six distinct regions indicated I–VI in Figs. 11(a)-(c) to highlight several stages of the hydration process. This was possible due to the short time interval between sweep measurements, allowing more detailed information than was previously available over the frequency range under consideration. Note that reference to the WetSEM images below mainly relates to Fig. 3 (and Video 1 in the electronic version of this article).

Region I: 0 – 20-min (WetSEM Images 1 and 2)

This region is characterised by a rapid increase in conductivity and a positive rate of change of conductivity (i.e. $d\sigma/dt$), with $d\sigma/dt$ decreasing with time. The increase in conductivity is attributed to the rapid dissolution of alkalis and sulphate (Na^+, K^+, Ca^{2+}, SO_4^{2-} and OH^-) into the aqueous phase and is accompanied by an increase in internal temperature as shown in Fig. 11(c). The reduction in $d\sigma/dt$ over this period would indicate that the surfaces of the cement grains are gradually covered by early hydration products thereby hindering the dissolution process, and hence an overall reduction in reaction rate. These physical changes were, however, not detectable in WetSEM study as such changes occur locally on the grain surface which was masked by the gauging water which is not electron transparent.

The rapid increase in $\varepsilon_N(\omega)$ (Fig. 11(b)) occurring concurrently at all selected frequencies mimics the rise in conductivity and would imply an increasing amount of charges developing on the grain surface, forming an electrical double layer (see Fig. 10(a)). Polarization of the double-layer can induce high permittivity values [40-42]; however, superimposed upon this polarization mechanism will be electrode polarization effects [43-45]. Electrode polarization is a low-frequency process which reduces with increasing frequency of applied field. At 1kHz, electrode effects will make a substantial contribution to the permittivity and it is only at higher frequencies ($\geq$100kHz) that the true bulk response will be revealed over this Region. Confirmation of this comes from the fact that $\varepsilon_{r,o}(\omega)$ (see Table 2) decreases by more than three orders of magnitude as the frequency increases by two decades

from 1kHz ($\varepsilon_{r,o} = 7.49\times10^{6}$) to 100kHz ($\varepsilon_{r,o} = 2.11\times10^{3}$) whereas $\varepsilon_{r,o}(\omega)$ changes by approximately one order of magnitude as the frequency increases by two decades from 100kHz to 1MHz ($\varepsilon_{r,o} = 1.42\times10^{2}$ at 1MHz). As the test frequency increases from 100kHz to 1MHz, it becomes more difficult for ions in the diffuse double-layer to follow the alternations of the electrical field which results in a reduction in permittivity with increasing frequency as presented in Table 2.

Region II: 20-min – 1-h 40-min (WetSEM Images 2 thru 4)

This region is characterised by a slower increase in conductivity and a reducing value of $d\sigma/dt$ (Fig. 11(a)). This implies that the dissolution process continues albeit at a reduced rate, possibly due to early hydrate formation around the cement grains such as ettringite and C-S-H [17, 36, 37]. Over this period, the internal temperature of the cement paste reduces, approaching the ambient temperature (Fig. 11(c)). Despite the initial growth on the cement grains, the ε_N response presented in Fig. 11(b) displays a similar trend to that of the conductivity implying that, at this w/c ratio, double-layer processes dominate over any reduction in charge mobility due to initial hydrate formation. Unfortunately, these physical changes are not evident under the WetSEM as they were masked by the gauging water. The conductivity and relative permittivity at all selected test frequencies reach their maximum values at the end of this Region.

Region III: 1-h 40-min – 2-h 10-min (WetSEM Images 4 and 5)

This is a short-lived region and marks a sudden reduction in conductivity, indicated by the change from a period of increasing conductivity to a period of decreasing conductivity over the remainder of the 24-h period. The decrease in conductivity within this region is very rapid as $d\sigma/dt$ reaches its global minimum (see Fig. 11(a)). It is now proposed that the sudden reduction in conductivity is associated with the crystallization of Portlandite infilling the water-filled capillary space between the grains as the time of occurrence of this Region coincides with the time of occurrence of Portlandite formation observed in the WetSEM study at 2-h 15-min (see Fig. 8). The slight difference in time is attributed to the fact that whilst the precipitation of Portlandite occurs within the entire volume of the

paste, only precipitates which are in contact with, or in close proximity to, the inner surface of the semi-electron-transparent membrane are detectable in the WetSEM and hence the apparent delay of its occurrence. Portlandite formation between the cement grains will limit the concentration of Ca^{2+} in the aqueous phase (or even result in a concentration reduction when the gypsum is depleted [46-47]) and in more discontinuous and tortuous electrolytic conduction pathways, both of which would have the effect of decreasing the overall conductivity. Video 2 in the electronic version of this article displays the time-lapse of Portlandite growth observed in Window 14 throughout the test period.

Occurring in parallel with the decrease in conductivity in Fig. 11(a) is a corresponding reduction in ε_N (see Fig. 11(b)). The reduction in polarizability of the paste (hence ε_r) is now attributed to the formation of Portlandite crystals within the microstructure which will reduce charge concentration and mobility. Despite the formation of Portlandite, the internal temperature of the paste over this Region continues to decrease, as shown in Fig. 11(c).

Region IV: 2-h 10-min – 8-h (WetSEM Images 5 thru 14)

From Fig. 11(a), the conductivity over this period continues to decrease whereas $d\sigma/dt$ remains relatively constant up to ~4-h, thereafter decreasing over the remainder of this Region. The decrease in $d\sigma/dt$ at ~4-h coincides with the increase in internal temperature at this time (Fig. 11(c)) which would indicate the start of a period of chemical activity. It is proposed that this feature is due to secondary reactions on the C_3S phase and the gradual formation of a more crystalline microstructure. The continual decrease in conductivity could be attributed to the continuous growth of Portlandite (see Figs. 3, 4(a) and (b), and Video 2) and C-S-H crystals (see Figs. 6(d), 7(a)-(f) and Video 4), causing an increase in rigidity of the paste.

In a similar fashion, Fig. 11(b) shows that the permittivity of the paste continues to decrease over this Region, although this decrease becomes less pronounced with increasing frequency. Indeed, over the period 4-h to 8-h, the permittivity at 500kHz and 1MHz starts to display a slight increase. At these

higher frequencies, it is expected that the increase in permittivity must involve a short-range movement of charges occurring locally on grain surfaces or at crystal boundary interfaces (see, for instance, Figs. 7(a)-(d) or Video 4). Regarding the latter, the increasing surface area of the cement grains due to the formation and outgrowth of ettringite and C-S-H crystals would increase the polarizability of the paste through enhanced double-layer and interfacial processes.

Region V: 8-h – 12.5-h (WetSEM Images 14 thru 22)

The conductivity continues to decrease although a *shoulder* occurs in the response which results in a local maximum on the $d\sigma/dt$ curve over the central portion of this Region and a local minimum at the end. Interestingly, at 100kHz and 250kHz, the permittivity also displays a local maximum, whereas at 500kHz and 1MHz the permittivity shows a continual increase over this Region. The conduction and polarization processes within the paste can result from several synergistic effects:

(i) the continuous growth of Portlandite and a more rapid outgrowth of fibrillar C-S-H crystals from the grain (see Figs. 7(e) and (f) or Video 4), resulting in an increase in surface area hence enhanced double-layer polarization on crystal surfaces. Conduction, on the other hand, would be reduced due to the development of more tortuous continuous pathways;

(ii) a release of ions into the capillary pore network through renewed chemical activity such as the transformation of AFt to AFm, with the subsequent release of Ca^{2+} and SO_4^{2-}, and reaction on the C_3A phases releasing alkalis bound up in them. This would increase conductive processes and enhance the polarizability of the paste through both interfacial and double-layer effects;

(iii) the accretion and infilling of the pore space by the products of hydration thereby forming a rigid structure which would serve to decrease both the conduction and polarizability of the paste due to space restriction and reduced charge mobility; and,

(iv) as the paste is hydrating under non-isothermal conditions, the increase in temperature would result in an increase in charge mobility, thereby increasing both polarization and conductive processes [48]. However, as the temperature rise within the paste is <1°C over this Region, this effect is considered negligible in comparison to the influence of (i)-(iii) above.

From the WetSEM study presented in Fig. 3 (images 14–22) and Video 1, it is evident that the intense chemical activity also has the effect of increasing water consumption thereby causing a reduction in the free water-content. This is estimated as occurring at ~8-h 25-min (see Fig. 8) and coincides with the beginning of Region V. It is interesting to note from images 14–22 in Fig. 3 and Figs. 4(b) and (c) that the growth of Portlandite over this Region did not displace the surrounding cement particles which were much smaller in size, indicating that the hydration products at this stage were sufficiently strong to hold the particulate material within the aqueous paste together. At the end of this region, the products of hydration (Portlandite and gel) have resulted in a percolated pore network thereby forming a rigid matrix.

Region VI: 12.5-h – end of test (WetSEM Images 22 thru 42)

This final region identified within the 24-h test period is characterized by a continual decrease in conductivity due to continued crystal growth and microstructural densification, resulting in a more tortuous, constricted and disconnected capillary pore network (see Videos 1–4). The ε_N response at 100kHz and 250kHz is similar to the conductivity as it displays a decreasing trend; however, at 500kHz and 1MHz, the permittivity increases with time. Regarding the increase in polarizability of the paste at 500kHz and 1MHz, this could result from increased interfacial processes at crystal boundary interfaces within the pore structure (see Fig. 10(b)), resulting from an increase in ionic concentrations in the pore fluid i.e. the continued release of ions from the AFt to AFm transformation. Interfacial polarization is a high frequency process and is only revealed – i.e. becomes more dominant over double-layer effects – as the frequency increases. As there is no detectable increase in conductivity caused by release of ions into the pore network, it would indicate that changes in the pore structure due to hydration are having a dominant influence on the conductivity of the paste than changes in pore-fluid chemistry.

4. Conclusions and Concluding Comments

Dual testing methodology utilizing electrical impedance measurements and WetSEM observations have been presented to provide information of the stages in the early hydration and complementary information on hydrate formation and crystal morphology. With regard to the impedance measurements, these were presented as conductivity (σ) and permittivity (ε_r), with the permittivity presented over the frequency range 1kHz–1MHz. The WetSEM observations were undertaken on a sealed vacuum-tight miniature capsule via 36, 300-μm square semi-electron-transparent windows and a novel, fully automated image collection technique was used to allow *in-situ* dynamic imaging under atmospheric conditions. The following conclusions can be drawn from this study:

1. The conductivity (σ), its rate of change $d\sigma/dt$ and the relative permittivity (ε_r) could be divided into six distinct regions which were used to identify key stages in the early hydration of cement paste. Over the frequency range 1kHz-1MHz, unlike the conductivity, the permittivity response changed markedly with electrode polarization processes dominant at low frequencies; however, at frequencies >100kHz the bulk response was revealed and related to double-layer and interfacial polarization processes occurring within the paste.
2. The WetSEM study revealed the nucleation of large, angular Portlandite crystals between the cement grains from ~2-h 15-min after gauging. This feature was coincident with the significant decrease in both conductivity and relative permittivity which took place at this time (viz, Region III).
3. The first half of Region IV is characterised by a reduction in conductivity and an almost constant $d\sigma/dt$ value. The decrease in conductivity could be associated with the continuous growth of Portlandite, as observed in the WetSEM study over the same period. This was then followed by a reduction in $d\sigma/dt$ (viz, become more negative) and an increase in internal temperature, indicating the start of a period of renewed chemical activity. During this period, a slight increase in permittivity at high frequencies (viz, 500kHz and 1MHz) was observed, occurring concurrently with the outgrowth of ettringite and C-S-H crystals from the WetSEM study. The increase in permittivity was as a result of the increase in the surface area of the

cement grains which increased the polarizability of the paste through enhanced double-layer and interfacial polarization processes.

4. The WetSEM study detected a reduction in the water-content of the paste at ~8-h 25-min after gauging which was coincident with the beginning of Region V identified from conductivity and relative permittivity measurements. The electrical measurements also underwent significant changes over Region V and explained in terms of dissolution processes and hydrate formation on grain surfaces.
5. Region VI is characterized by a continual decrease in internal temperature, conductivity and $d\sigma/dt$ due to continued crystal growth and microstructural densification, as observed in the WetSEM study.

Acknowledgements

The authors gratefully acknowledge the support of the School of Energy, Geoscience, Infrastructure and Society for placing the facilities of the School at their disposal. Datasets from this study are available upon request from the lead author (b.suryanto@hw.ac.uk).

References

[1] D.D. Double, A. Hellawell, S.J. Perry, The hydration of Portland cement, Proc. R. Soc. Lond. A., Vol. 359, Mar. 1978, pp. 435–451.

[2] K.A. Paine, L. Zheng, R.K. Dhir, Experimental study and modelling of heat evolution of blended cements, Adv. Cem. Res. 17 (3) (2005) 121–132.

[3] L. Wadsö, M. Arndt, An international round robin test on isothermal (conduction) calorimetry for measurement of three-day heat of hydration of cement, Cem. Concr. Res. 79 (2016) 316–322.

[4] A. Arora, G. Sant, N. Neithalath, Ternary blends containing slag and interground/blended limestone: Hydration, strength, and pore structure, Const. Build. Mater. 102 (1) (2016) 113–124.

[5] T. Kishi, K. Maekawa, Multi-component model for hydration heating of Portland cement, Concr. Lib. JSCE 28 (1) (1996) 97–115.

[6] G.H. An, J.M. Park, S.L. Cha, J.K. Kim, Development of a portable device and compensation method for the prediction of the adiabatic temperature rise of concrete, Constr. Build. Mater. 102 (1) (2016) 640–647.

[7] D.A. Lange, K. Sujata, H.M. Jennings, Observations of wet cement using electron microscopy, Ultramicroscopy 37 (1–4) (1991) 234–238.

[8] K.L. Scrivener, Microscopy methods in cement and concrete science, World Cem. 28 (9) (1997) 121–126.

[9] D. Gastaldi, F. Canonico, L. Capelli, E. Boccaleri, M. Milanesio, L. Palin, G. Croce, F. Marone, K. Mader, M. Stampanoni, In situ tomographic investigation on the early hydration behaviors of cementing systems, Constr. Build. Mater. 29 (2012) 284–290.

[10] Z. Liu, Y. Zhang, G. Sun, Q. Jiang, Observation of microstructure formation process of cement paste using non-destructive methods, Mag. Concr. Res. 64 (11) (2012) 957–965.

[11] C. Hu, Y. Han, Y. Gao, Y. Zhang, Z. Li, Property investigation of calcium–silicate–hydrate (C–S–H) gel in cementitious composites, Mater. Charact. 95 (2014) 129–139.

[12] C.A. da Luz, R.D. Hooton, Influence of curing temperature on the process of hydration of supersulfated cements at early age, Cem. Concr. Res. 77 (2015) 69–75.

[13] M. Moradian, H. Qinang, M. Aboustait, M.T. Ley, J.C. Hanan, X. Xiao, G.W. Scherer, Z. Zhang, Direct observation of void evolution during cement hydration, Mater. Des. 136 (2017) 137–149.

[14] O. Wenzel, M. Schwotzer, E. Müller, V.S.K. Chakravadhanula, T. Scherer, A. Gerdes, Investigating the pore structure of the calcium silicate hydrate phase, Mater. Charact. 133 (2017) 133–137.

[15] Z. Zhang, G.W. Scherer, A. Bauer, Morphology of cementitious material during early hydration, Cem. Concr. Res. 107 (2018) 85–100.

[16] A. Katz, A. Bentur, K. Kovler, A novel system for in-situ observations of early hydration reactions in wet conditions in conventional SEM, Cem. Concr. Res. 37 (1) (2007) 32–37.

[17] M. Fylak, J. Goske, W. Kachler, R. Wenda, H. Pollmann, Cryotransfer scanning electron microscopy for the study of cementitious systems, Microscopy Anal. 114 (2006) 9–12.

602 [18] A. Zingg, L. Holzer, A. Kaech, F. Winnefeld, J. Pakusch, S. Becker, L. Gauckler, The
603 microstructure of dispersed and non-dispersed fresh cement pastes–new insight by cryo-microscopy,
604 Cem. Concr. Res. 38 (4) (2008) 522–529.
605 [19] C.S. Deng, C. Breen, J. Yarwood, S. Habesch, J. Phipps, B. Craster, G. Maitland, Ageing of
606 oilfield cement at high humidity: a combined FEG-ESEM and Raman microscopic investigation, J.
607 Mater. Chem. 12 (10) (2002) 3105–3112.
608 [20] G. Ye, J. Hu, K. van Breugel, P. Stroeven, Characterization of the development of microstructure
609 and porosity of cement-based materials by numerical simulation and ESEM image analysis, Mater.
610 Struct. 35 (10) (2002) 603–613.
611 [21] Y. Sakalli, R. Trettin, Investigation of C3S hydration by environmental scanning electron
612 microscope, J. Microscopy 259 (1) (2015), 53–58.
613 [22] S. Atkinson, Novel membrane-related technologies aid biological analyses, Membr. Tech. 5
614 (2004) 5–7.
615 [23] S. Thiberge, A. Nechushtan, D. Sprinzak, O. Gileadi, V. Behar, O. Zik, Y. Chowers, S. Michaeli,
616 J. Schlessinger, E. Moses, Scanning electron microscopy of cells and tissues under fully hydrated
617 conditions, Proc. Natl. Acad. Sci. USA, Vol. 101, No. 10, 2004, pp. 3346–3351.
618 [24] J.C. Molero, S. Lee, I. Leizerman, A. Chajut, A. Cooper, K. Walder, Effects of rosiglitazone on
619 intramyocellular lipid accumulation in Psammomys obesus, BBA-Mol. Basis Dis. 1802 (2) (2010)
620 235–239.
621 [25] E. Gallucci, K. Scrivener, In situ dynamic SEM imaging of hydration of cement using WETSEM
622 technology, Adv. Appl. Ceram. 106 (6) (2007) 319–326.
623 [26] G. Venkiteela, Z. Sun, In situ observation of cement particle growth during setting, Cem. Concr.
624 Compos. 32 (3) (2010) 211–218.
625 [27] H.M. Taha, W.J. McCarter, B. Suryanto, G. Starrs, Frequency- and time-domain dependency of
626 electrical properties of cement-based materials during early hydration, ASTM Adv. Civ. Eng. Mat. 6
627 (2) (2017) 65–83.
628 [28] B. Suryanto, W.J. McCarter, G. Starrs, T.M. Chrisp, Characterization of fly-ash using
629 electrochemical impedance spectroscopy, Procedia Eng. 171 (2017) 705–714.

630 [29] W.J. McCarter, T.M. Chrisp, G. Starrs, A. Adamson, E. Owens, P.A.M Basheer, S.V.
631 Nanukuttan, S. Srinivasan, N. Holmes, Developments in performance monitoring of concrete exposed
632 to extreme environments, ASCE J. Infra. Sys. 18 (3) (2011) 167–175.
633 [30] British Standards Institution (BSI), EN197-1:2000, Cement-Part 1: Composition, specifications
634 and conformity criteria for common cements, BSI, London, 2000.
635 [31] B. Suryanto, J.O. Buckman, P. Thompson, M. Bolbol, W.J. McCarter, Monitoring micro-crack
636 healing in an engineered cementitious composite using the environmental scanning electron
637 microscope, Mater. Charact. 119 (2016) 175–185.
638 [32] B.J. Christensen, R.T. Coverdale, R.A. Olson, S.J. Ford, E.J. Garboczi, H.M. Jennings, T.0.
639 Mason, Impedance spectroscopy of hydrating cement-based materials: measurement, interpretation,
640 and application, J. Am. Ceram. Soc. 77 (11) (1994) 2789–2804.
641 [33] W.J. McCarter, The a.c. impedance response of concrete during early hydration, J. Mater. Sci. 31
642 (1996) 6285–6292.
643 [34] W.J. McCarter, G. Starrs, T.M. Chrisp, Electrical monitoring methods in cement science, in: P.
644 Barnes and J. Bensted (Eds.), Structure and Performance of Cements, Second Edition, Spon Press,
645 London 2002, pp. 442–456 (ISBN 0-203-47778-2).
646 [35] B. Suryanto, W.J. McCarter, G. Starrs, G.V. Ludford-Jones, Electrochemical immittance
647 spectroscopy applied to a hybrid PVA/steel fiber engineered cementitious composite, Mater. Des. 105
648 (2016) 179–189.
649 [36] R. Ylmén, U. Ulf, B.M. Steenari, I. Panas, Early hydration and setting of Portland cement
650 monitored by IR, SEM and Vicat techniques, Cem. Concr. Res. 39 (5) (2009) 433–439.
651 [37] G.L. Golewsgi. Improvement of fracture toughness of green concrete as a result of addition of
652 coal fly ash. Characterization of fly ash microstructure, Mater. Charact. 134 (2017) 335–346.
653 [38] N.B. Winter, ‘Scanning Electron Microscopy of Cement and Concrete’, WHD Microanalysis,
654 Woodbridge, Suffolk, 2012.
655 [39] C. Famy, A.R. Brough, H.F.W. Taylor, The CSH gel of Portland cement mortars: Part I. The
656 interpretation of energy-dispersive X-ray microanalyses from scanning electron microscopy, with

some observations on CSH, AFm and AFt phase compositions, Cem. Concr. Res. 33 (9) (2003) 1389–1398.

[40] H.P. Schwan, G. Schwarz, J. Maczuk, H. Pauly, On the low-frequency dielectric dispersion of colloidal particles in electrolyte solution, J. Phys. Chem. 66 (12) (1962) 2626–2635.

[41] G. Schwarz, G., A theory of the low-frequency dielectric dispersion of colloidal particles in electrolyte solution, J. Phys. Chem. 66 (12) (1962) 2636–2642.

[42] J.B. Hasted, Aqueous Dielectrics, Chapman and Hall, London, 1973.

[43] A. Serghei, M. Tress, J.R. Sangoro, F. Kremer, Electrode polarization and charge transport at solid interfaces, Phys. Rev. B 80 (18) (2009), 184301.

[44] P.B. Ishai, M.S. Talary, A. Caduff, E. Levy, Y. Feldman, Electrode polarization in dielectric measurements: a Review, Meas. Sci. Tech. 24 (10) (2013) 102001 1–21.

[45] W.J. McCarter, H.M. Taha, B. Suryanto, G. Starrs, Two-point concrete resistivity measurements: interfacial phenomena at the electrode–concrete contact zone, Meas. Sci. Technol. 26 (8) (2015) 085007 1–13.

[46] B. Lothenbach, F. Winnefeld. Thermodynamic modelling of the hydration of Portland cement, Cem. Concr. Res. 36 (2) (2006) 209–226.

[47] Y. Elakneswaran, T. Ishida, Development and verification of an integrated physicochemical and geochemical modelling framework for performance assessment of cement-based materials, J. Adv. Concr. Technol. 12 (2014) 111–126.

[48] W.J. McCarter, Effects of temperature on conduction and polarization in Portland cement mortar, J. Am. Ceram. Soc. 78 (2) (1995) 411–415.

685 **Figure captions**

686

687 **Fig. 1.** (a) Schematic of the Quantomix capsule; (b) close-up of the top windows numbered according
688 to their position, with the prefix representing the row number and the suffix representing the column
689 number; (c) test cell for electrical measurements; and (d) layout of tile numbered according to the
690 sequence of image collection, overlain on the windows shown in (b).

691

692 **Fig. 2.** Stitched BSE images showing the progress of cement hydration on all windows: (a) 30-min;
693 (b) 4.5-h; (c) 12-h and (d) 18-h after gauging.

694

695 **Fig. 3.** Time-lapse imaging of Window 14 (3-6 on Fig. 1(b)) with images taken every ~35-min over
696 the initial 24-h after gauging. Images are arranged from left-to-right and top-to-bottom in the order of
697 measurement sequence, with each row displaying successive changes over a ~3-hour period. Each
698 window is 300□m square.

699

700 **Fig. 4.** Enlarged BSE images of the progressive formation of Portlandite crystals indicated by the
701 rectangles in Fig. 3 at (a) ~4-h (image 8), (b) ~8-h (image 14), (c) ~12-h (image 21) and (d) ~18-h
702 (image 32). (e) and (f) are enlarged images of areas indicated by the circles on image 14 in Fig. 3
703 where the first indication of a reduction in water-content is evident.

704

705 **Fig. 5.** Selected time-lapse images of Window 2 (1-4 on Fig. 1(b)) at (a) the initial state, (b) 6-h, (c) 8-
706 h, (d) 10-h, (e) 12-h and (f) 24-h after gauging. The bright dots at the initial state are the upper part of
707 the cement particles while the dark areas represent the interstitial aqueous phase. A porous surface is
708 evident as the water-level has reduced, revealing partially hydrated cement grains which are bright
709 and capillary pores which are much darker.

710 **Fig. 6.** Enlarged images of selected areas of Window 2 (indicated on Fig. 5(f)) taken at 24 hours after
711 gauging showing the presence of: (a) and (b) large Portlandite crystal surrounded by cement grains

712 covered by fibrillar outgrowths comprising C-S-H and some longer needle-like (ettringite) crystals;
713 (c) and (d) smaller hydration products where the Portlandite crystal is absent.
714
715 **Fig. 7.** Time-lapse images of Fig. 6(d) at (a) 2.5-h; (b) 4-h; (c) 6.5-h; (d) 8-h; (e) 10-h; and (f) 12.5-h
716 after gauging.
717
718 **Fig. 8.** Observed time of the first appearance of Portlandite crystals and the first indication of a
719 reduction in water-content resulting from hydration reactions. The mean values are indicated in the
720 Figure by the dashed lines.
721
722 **Fig. 9.** (a) BSE images of Windows 11, 12, 17, 18, 24 and 25 (see Fig. 1(d)) after 24-h hydration; (b)
723 respective EDX maps of Windows after 24-h hydration where red represents potassium, green is
724 sulphur, yellow is calcium, pink is silicon and cyan represents areas rich in aluminum; (c) is enlarged
725 image of rectangle indicated on Window 18 in (a) with the respective EDX map shown in (d); green
726 represents areas rich in aluminum, yellow is calcium and cyan is silicon; and (e) is typical elemental
727 composition of selected areas in (d). These figures appear in colour in the electronic version.
728
729 **Fig. 10.** Schematic showing (a) double layer polarization and (b) interfacial polarization.
730
731 **Fig. 11.** (a) Conductivity, □, and its derivative, d□/dt, during initial 24-hours, with Regions I–VI
732 indicated; (b) normalized relative permittivity, □$_N$, at five selected spot frequencies; and (c) variation
733 in internal temperature of cement paste.
734
735
736
737
738
739

Video Captions

Video 1. Animation of Window 14 (3-6 on Fig. 1(b)) displaying Portlandite formation and general microstructural densification over the 24-h test period.

Video 2. Animation of Portlandite growth in Window 14 over the 24-h test period.

Video 3. Animation of Window 2 (1-4 on Fig. 1(b)) where fewer numbers of Portlandite precipitates are evident over the 24-h test period.

Video 4. Animation of precipitates on grain surfaces within the area indicated by the rectangle in Fig. 5(f) over the 24-h test period.

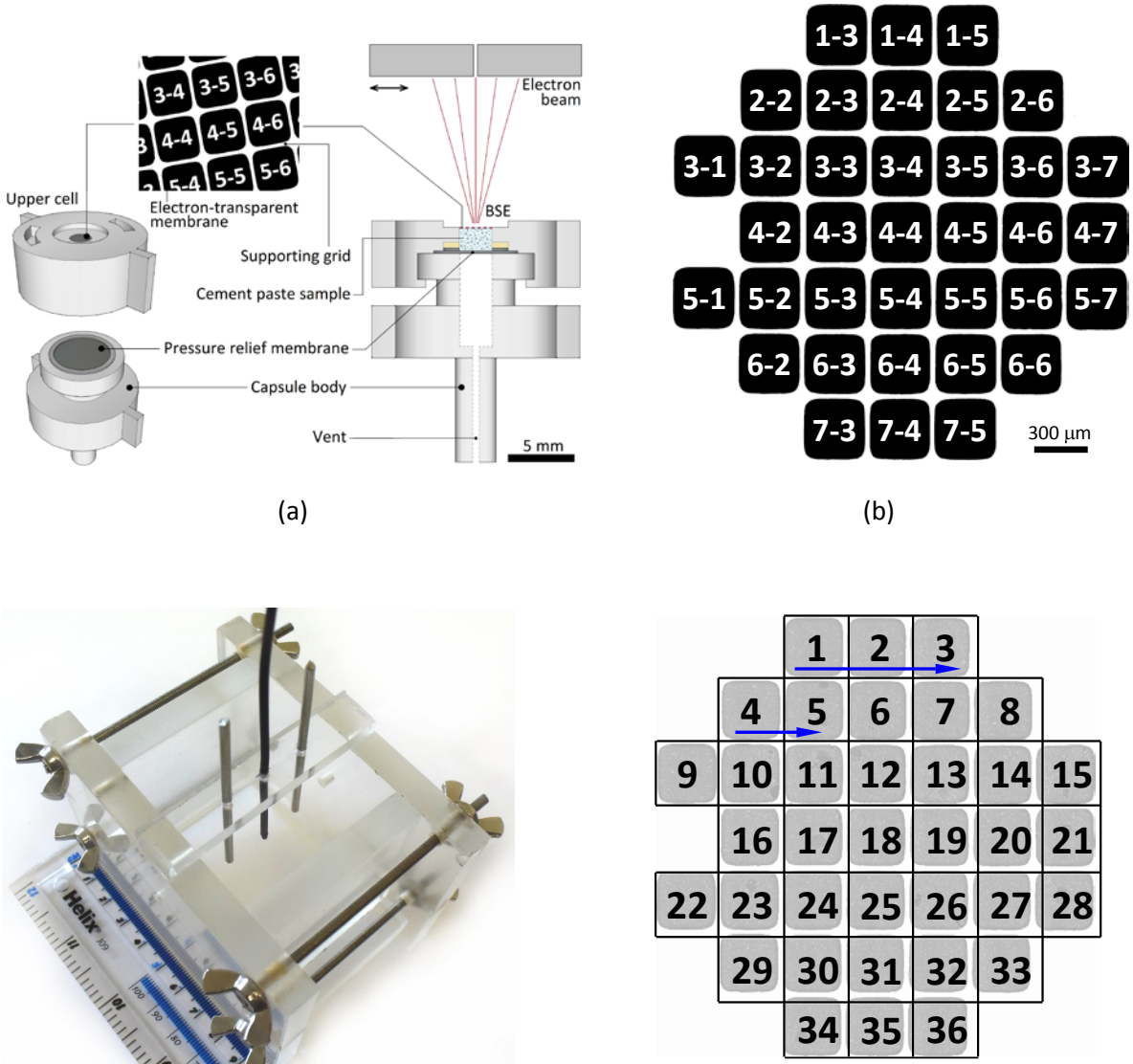

Fig. 1. (a) Schematic of the Quantomix capsule; (b) close-up of the top windows numbered according to their position, with the prefix representing the row number and the suffix representing the column number; (c) test cell for electrical measurements; and (d) layout of tile numbered according to the sequence of image collection, overlain on the windows shown in (b).

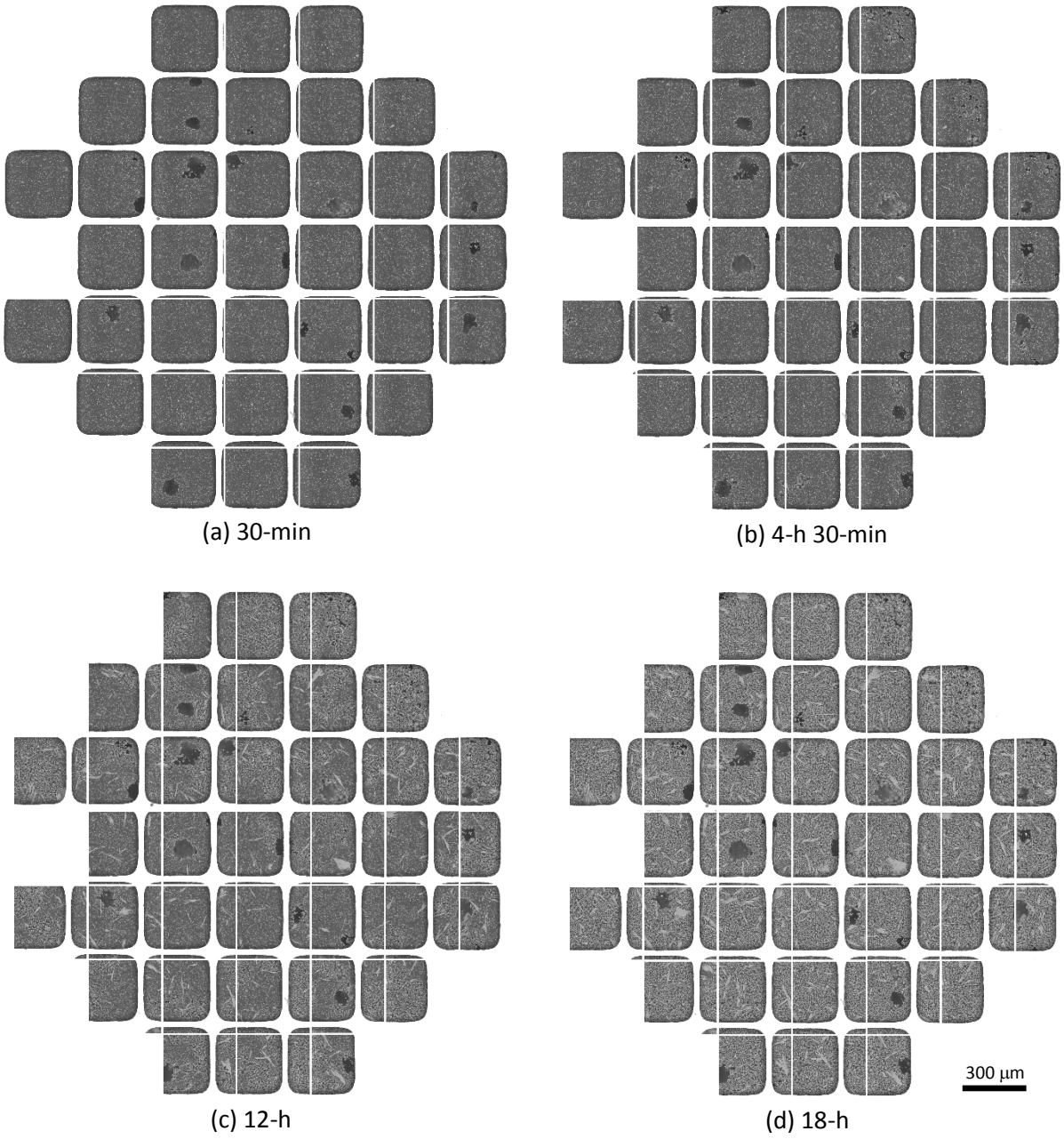

Fig. 2. Stitched BSE images showing the progress of cement hydration on all windows: (a) 30-min; (b) 4.5-h; (c) 12-h and (d) 18-h after gauging.

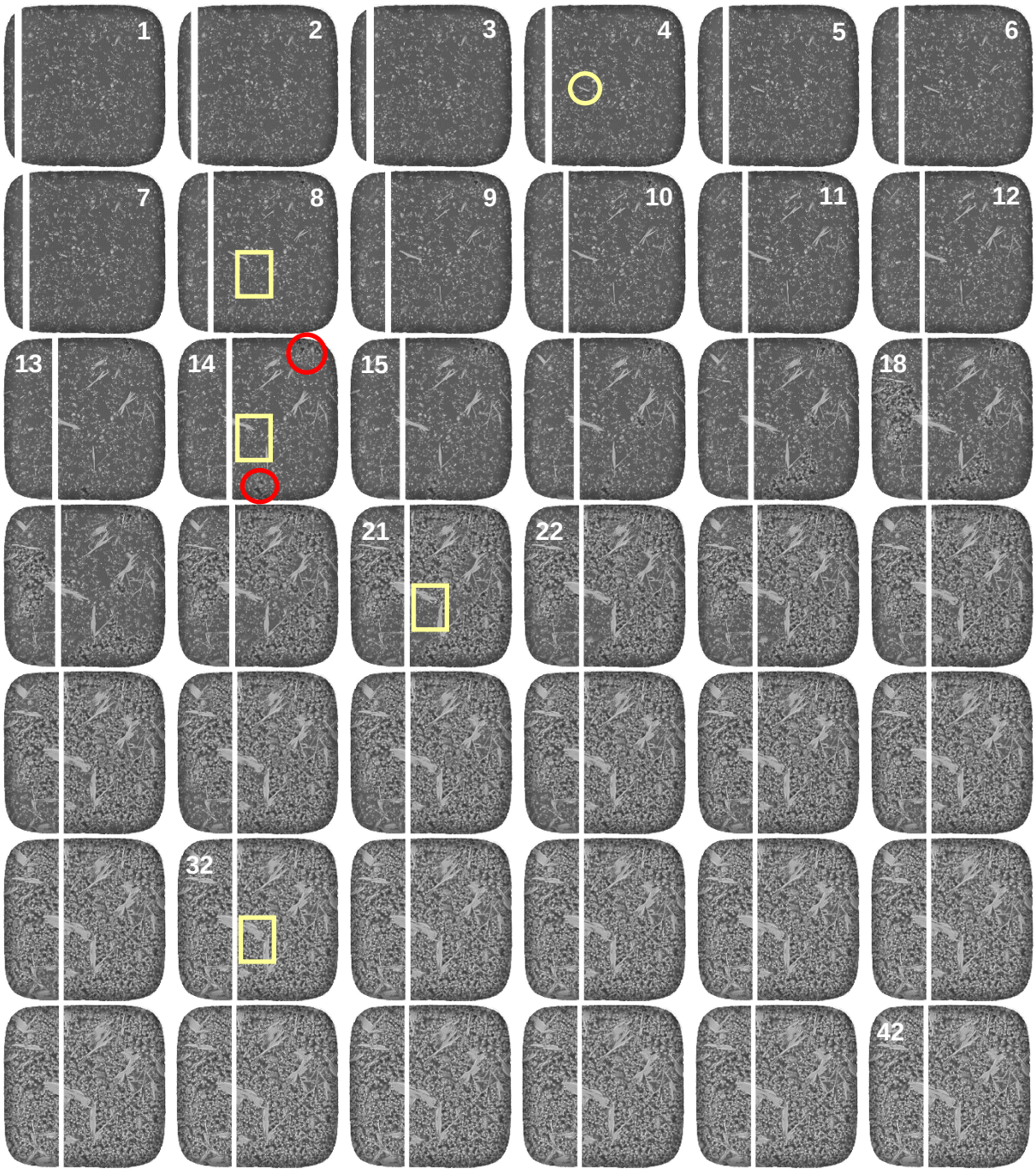

Fig. 3. Time-lapse imaging of Window 14 (3-6 on Fig. 1(b)) with images taken every ~35-min over the initial 24-h after gauging. Images are arranged from left-to-right and top-to-bottom in the order of measurement sequence, with each row displaying successive changes over a ~3-hour period. Each window is 300μm square.

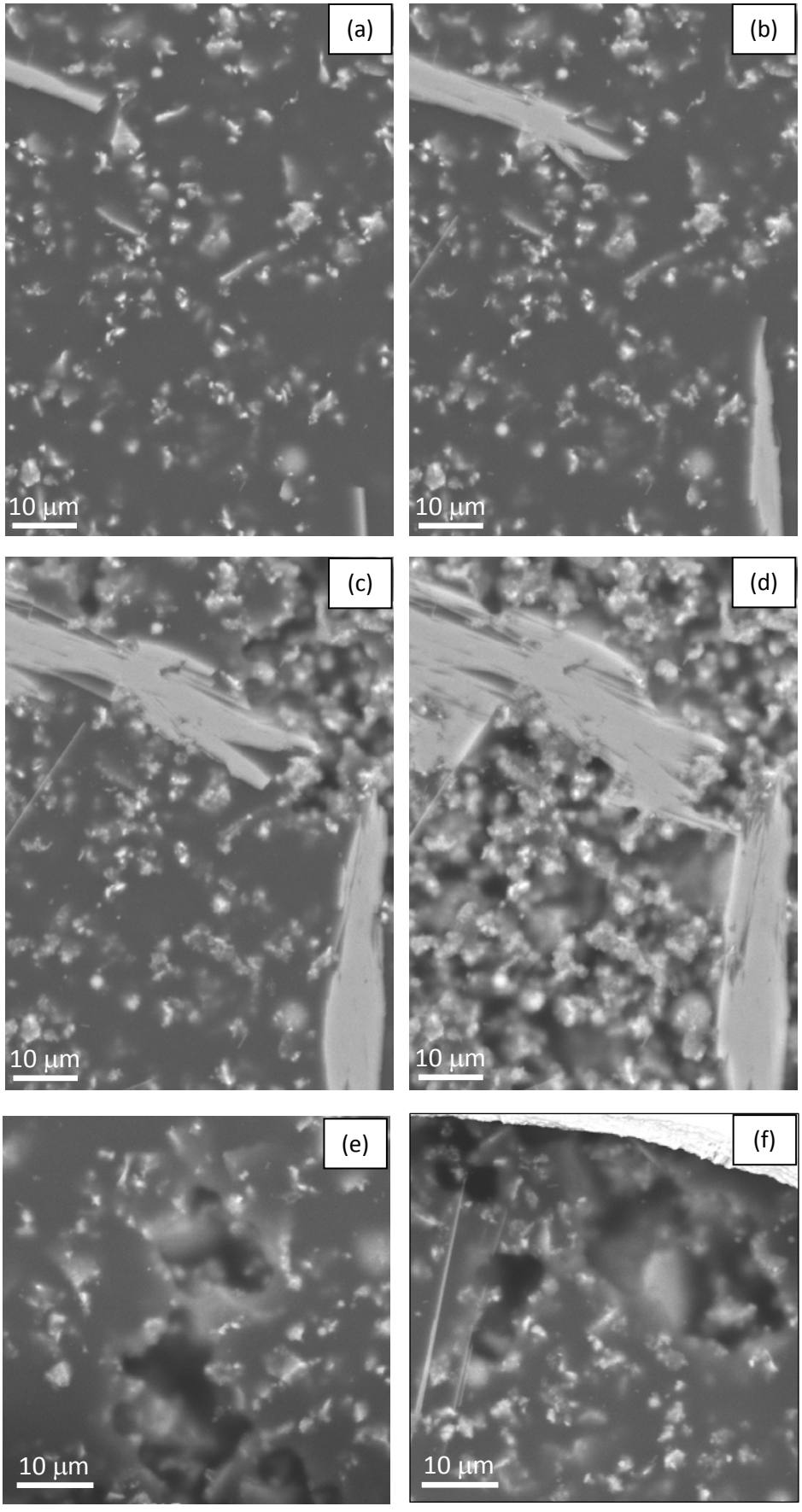
(a)
10 μm
(b)
10 μm
(c)
10 μm
(d)
10 μm
(e)
10 μm
(f)
10 μm

826 **Fig. 4.** Enlarged BSE images of the progressive formation of Portlandite crystals indicated by the
827 rectangles in Fig. 3 at (a) ~4-h (image 8), (b) ~8-h (image 14), (c) ~12-h (image 21) and (d) ~18-h
828 (image 32). (e) and (f) are enlarged images of areas indicated by the circles on image 14 in Fig. 3
829 where the first indication of a reduction in water-content is evident.

830

831

832

833

834

835

836

837

838

839

840

841

842

843

844

845

846

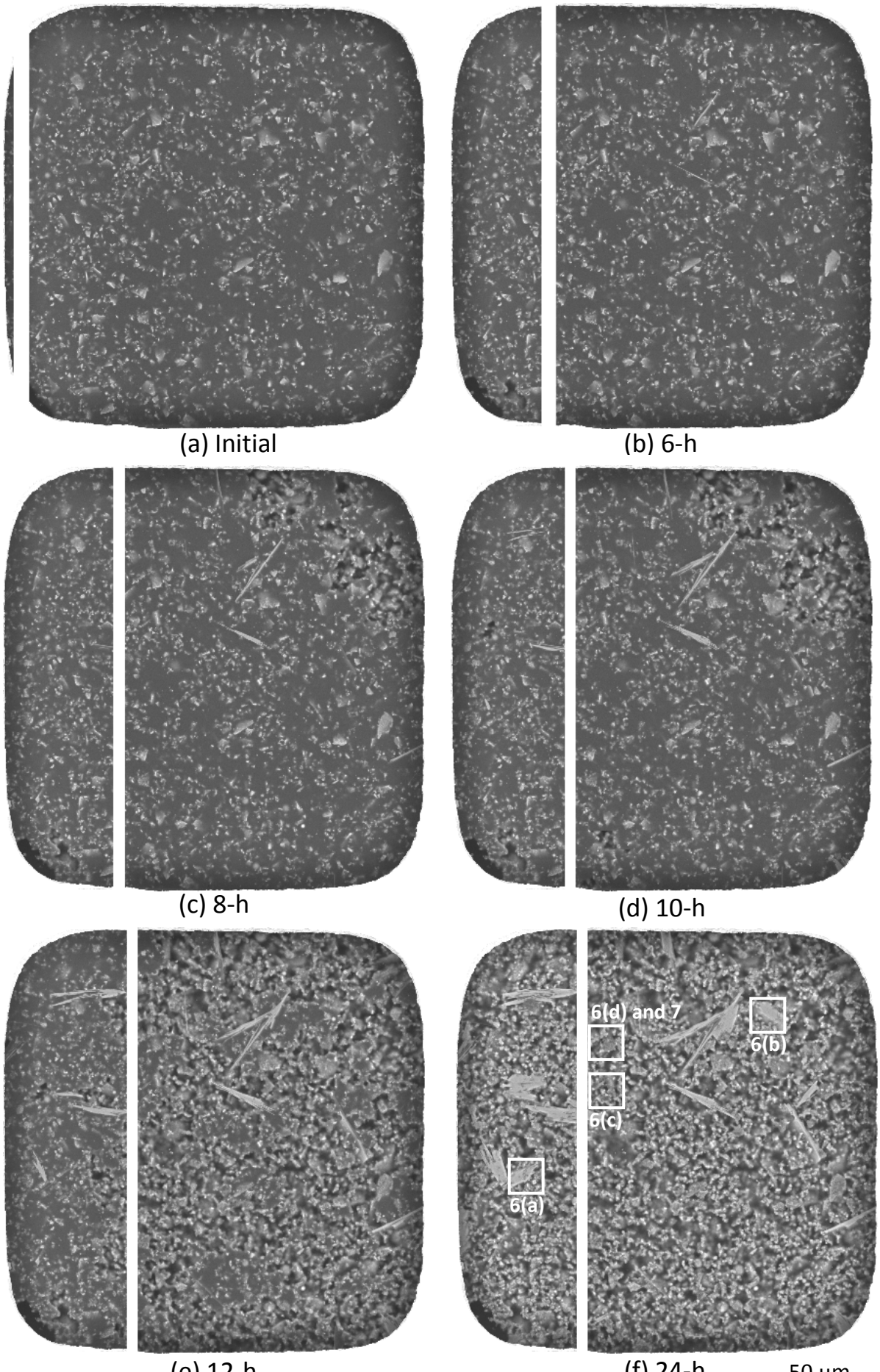
(a) Initial
(b) 6-h
(c) 8-h
(d) 10-h
(e) 12-h
(f) 24-h
6(d) and 7
6(b)
6(c)
6(a)
50 μm

Fig. 5. Selected time-lapse images of Window 2 (1-4 on Fig. 1(b)) at (a) the initial state, (b) 6-h, (c) 8-h, (d) 10-h, (e) 12-h and (f) 24-h after gauging. The bright dots at the initial state are the upper part of the cement particles while the dark areas represent the interstitial aqueous phase. A porous surface is evident as the water-level has reduced, revealing partially hydrated cement grains which are bright and capillary pores which are much darker.

878

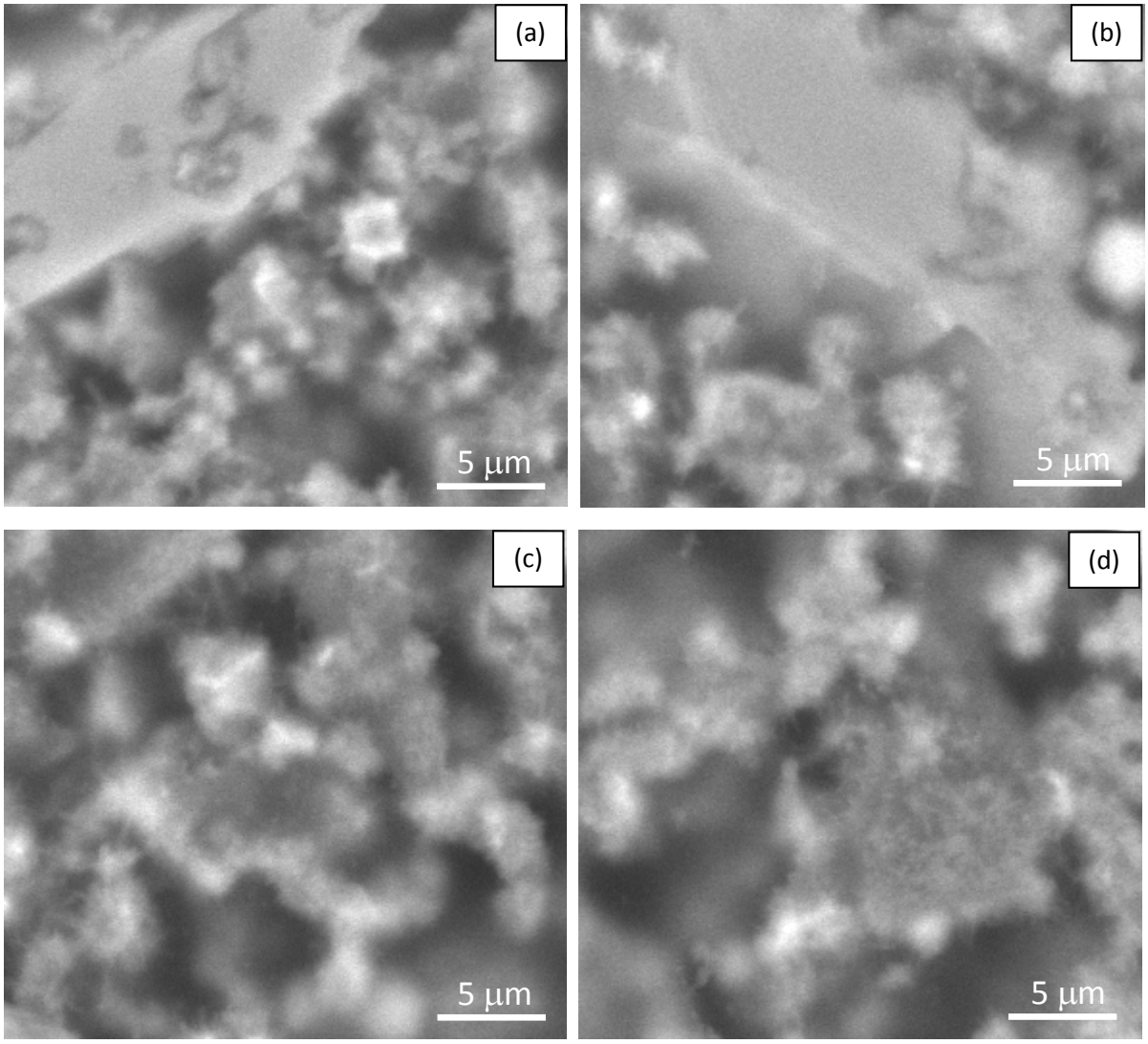

879

880

881 **Fig. 6.** Enlarged images of selected areas of Window 2 (indicated on Fig. 5(f)) taken at 24 hours after
882 gauging showing the presence of: (a) and (b) large Portlandite crystal surrounded by cement grains
883 covered by fibrillar outgrowths comprising C-S-H and some longer needle-like (ettringite) crystals; (c)
884 and (d) smaller hydration products where the Portlandite crystal is absent.

885

886

887

888

889

890

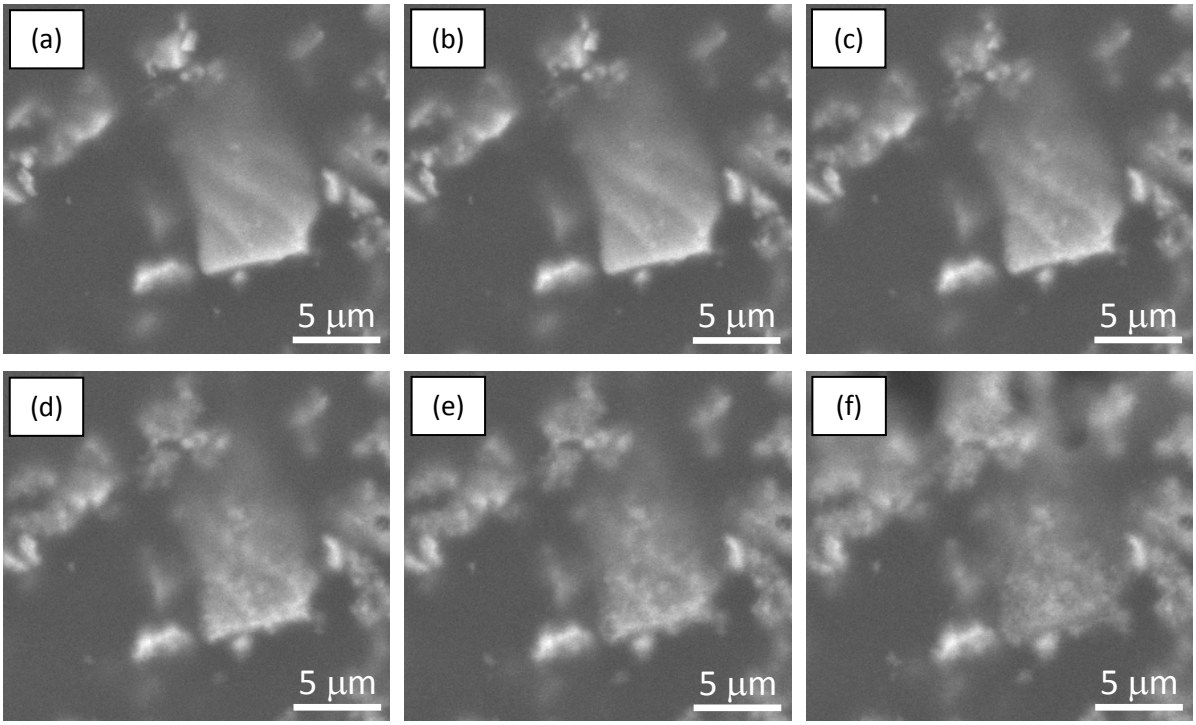

Fig. 7. Time-lapse images of Fig. 6(d) at (a) 2.5-h; (b) 4-h; (c) 6.5-h; (d) 8-h; (e) 10-h; and (f) 12.5-h after gauging.

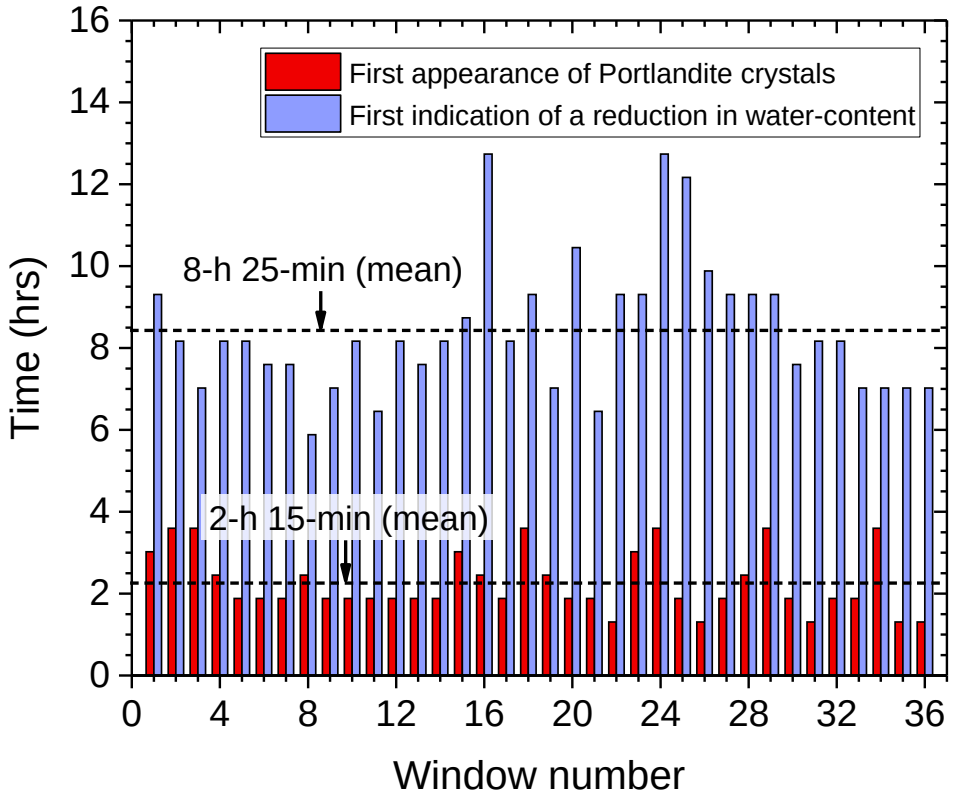

Fig. 8. Observed time of the first appearance of Portlandite crystals and the first indication of a reduction in water-content resulting from hydration reactions. The mean values are indicated in the Figure by the dashed lines.

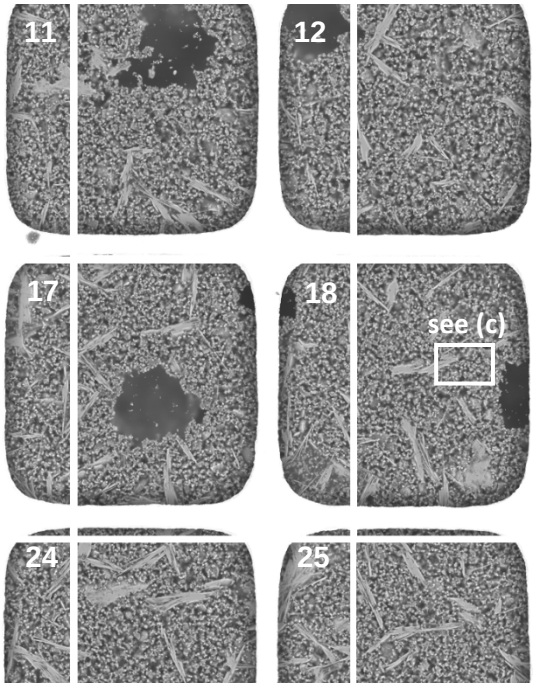

(a)

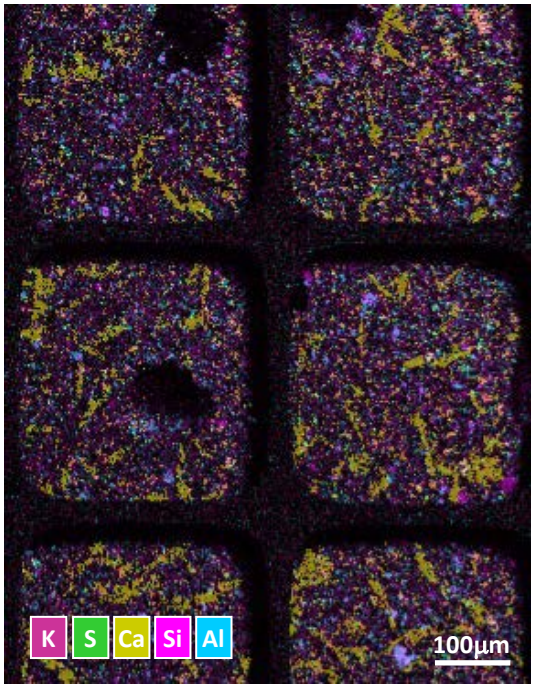

(b)

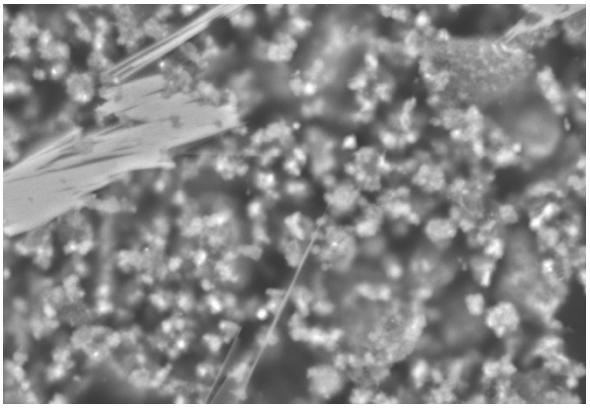

(c)

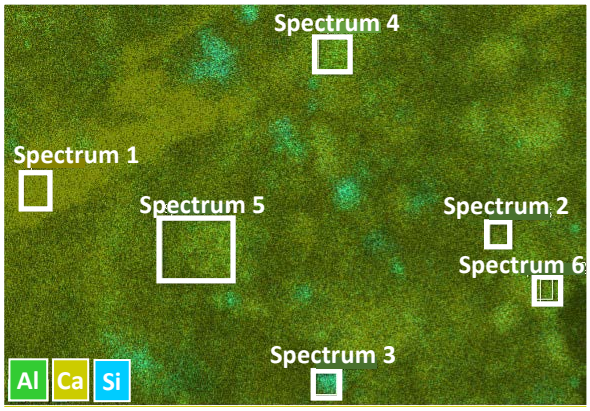

(d)

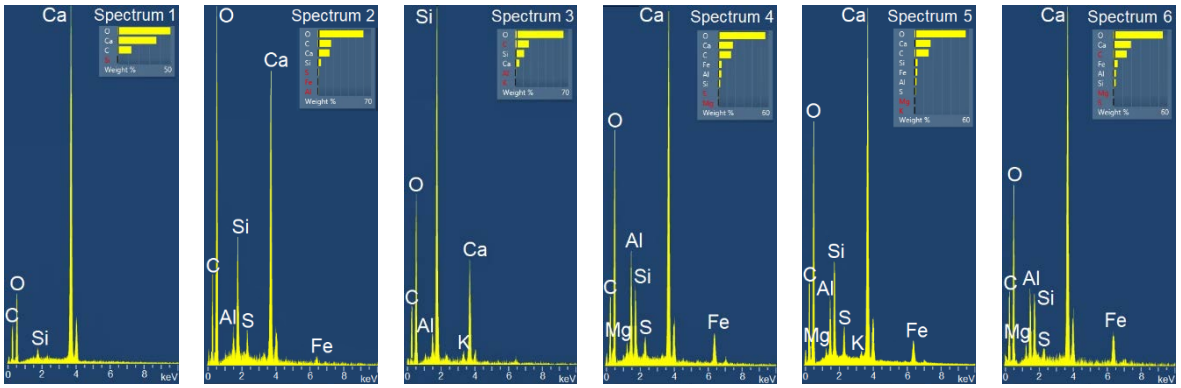

(e)

Fig. 9. (a) BSE images of Windows 11, 12, 17, 18, 24 and 25 (see Fig. 1(d)) after 24-h hydration; (b) respective EDX maps of Windows after 24-h hydration where red represents potassium, green is

sulphur, yellow is calcium, pink is silicon and cyan represents areas rich in aluminum; (c) is enlarged image of rectangle indicated on Window 18 in (a) with the respective EDX map shown in (d); green represents areas rich in aluminum, yellow is calcium and cyan is silicon; and (e) is typical elemental composition of selected areas in (d). These figures appear in colour in the electronic version.

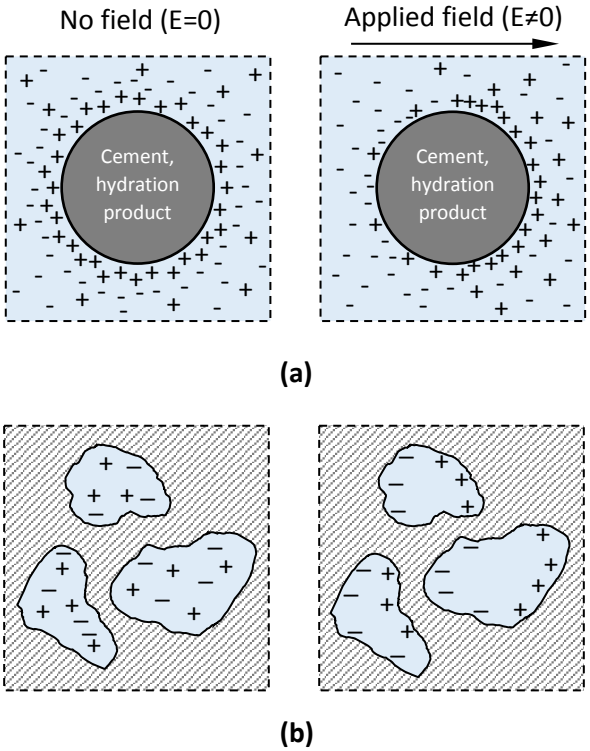

Fig. 10. Schematic showing (a) double layer polarization and (b) interfacial polarization.

962

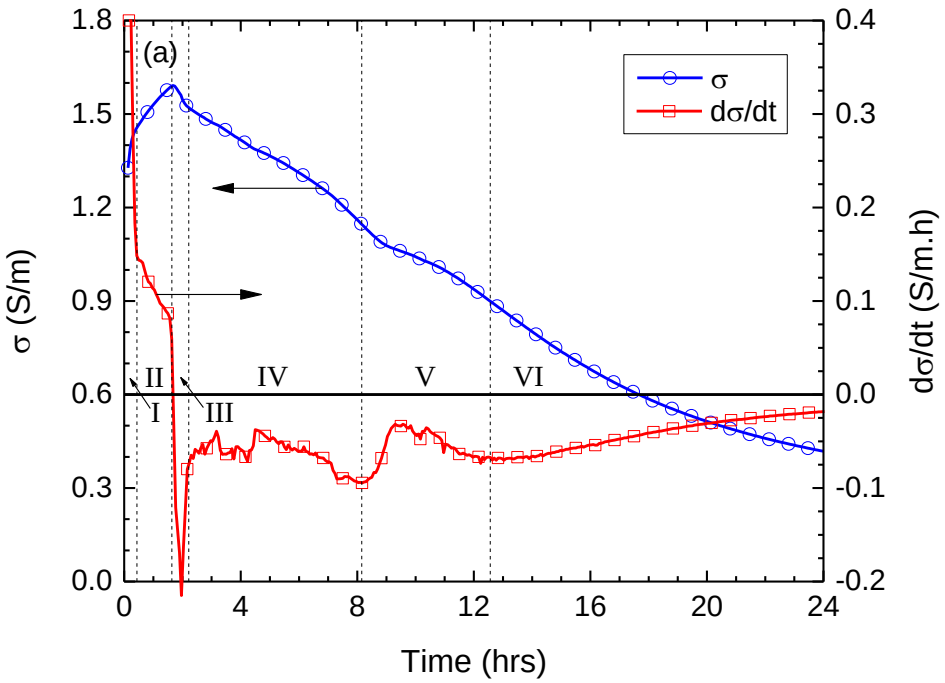

963

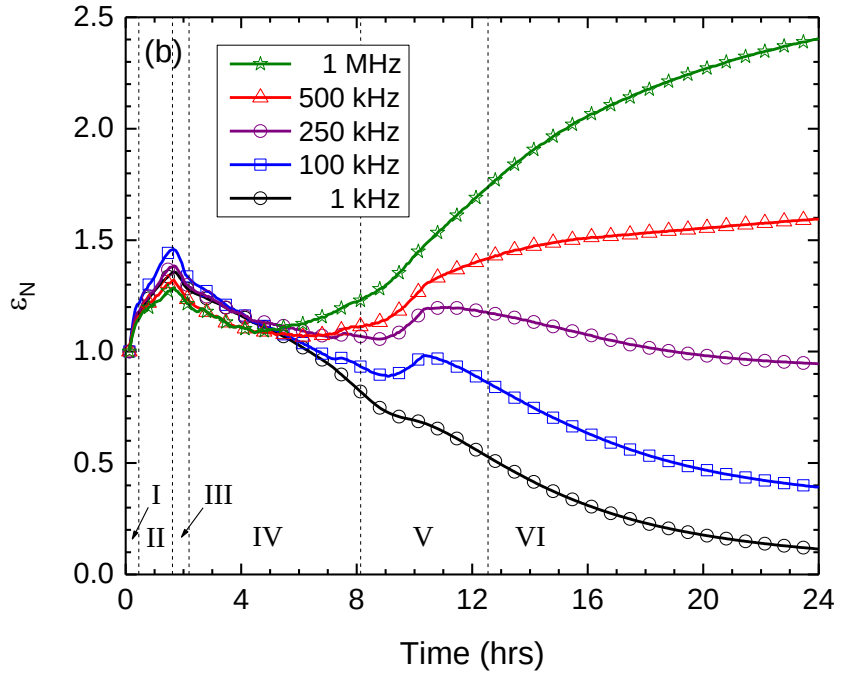

964

965

966

967

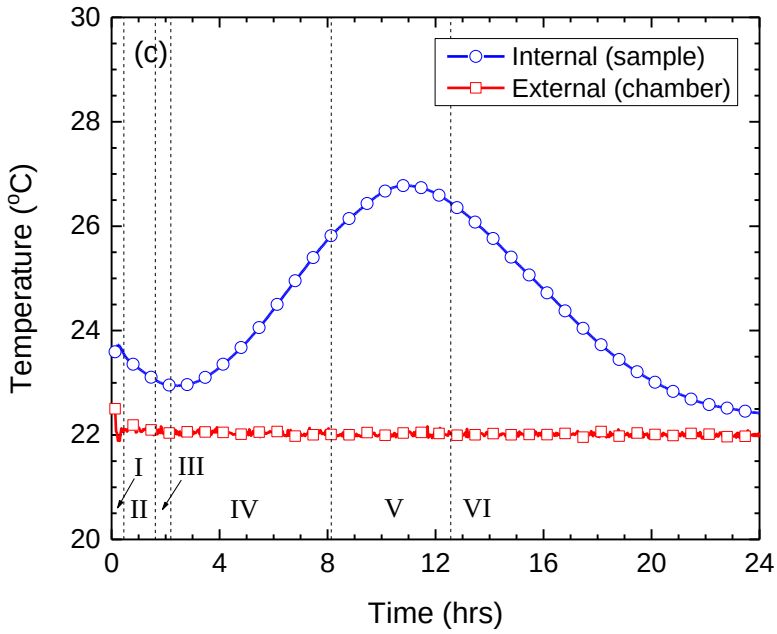

968

969 **Fig. 11.** (a) Conductivity, σ, and its derivative, dσ/dt, during initial 24-hours, with Regions I–VI
970 indicated; (b) normalized relative permittivity, ε_N, at five selected spot frequencies; and (c) variation
971 in internal temperature of cement paste.

972

973

974

975

976

977

978

979

980

981

982

983

Video thumbnails

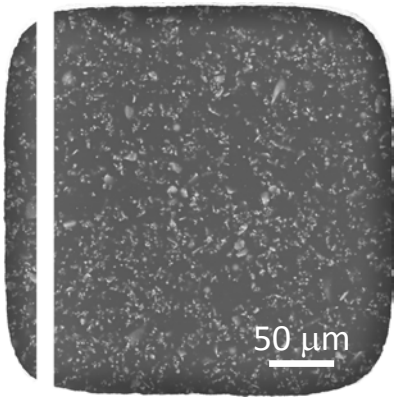

Thumbnail image for **Video 1**

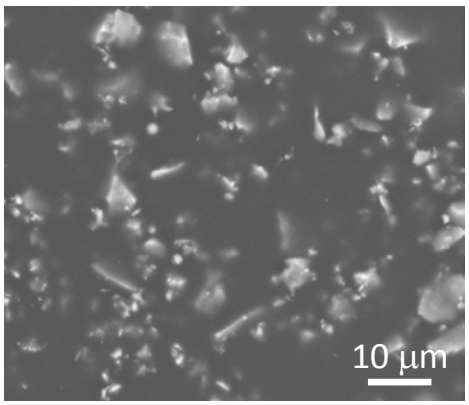

Thumbnail image for **Video 2**

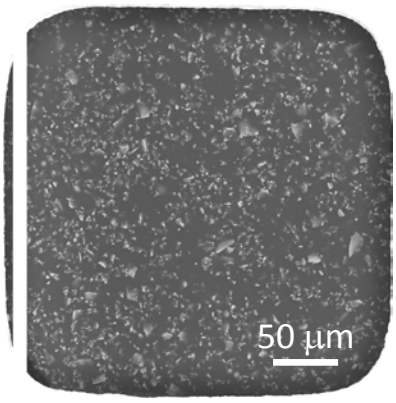

Thumbnail image for **Video 3**

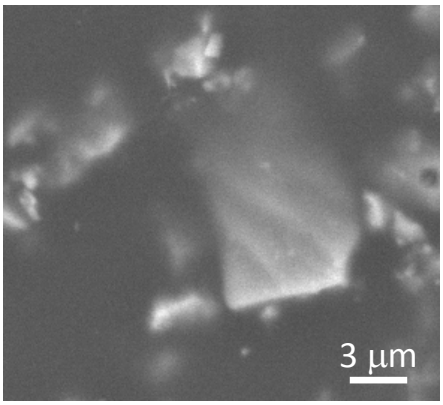

Thumbnail image for **Video 4**

Table captions

Table 1. Typical oxide analysis of the cement.

Table 2. Initial values of relative permittivity, $\varepsilon_{r,o}(\omega)$, at selected five spot frequencies.

1019 **Table 1**. Typical oxide analysis of the cement.

Content	By weight (%)
SiO_2	20.95
Al_2O_3	5.20
Fe_2O_3	3.42
CaO	59.86
MgO	2.25
K_2O	0.56
Na_2O	0.21

1020

1021 **Table 2**. Initial values of relative permittivity, $\varepsilon_{r,o}(\omega)$, at selected five spot frequencies.

Frequency (kHz)	$\varepsilon_{r,o}(\omega)$
1	7.49×10^{6}
100	2.11×10^{3}
250	5.45×10^{2}
500	2.50×10^{2}
1,000 (1 MHz)	1.42×10^{2}

1022